PHYSICAL REVIEW C **93**, 044306 (2016)

Mapping the deformation in the "island of inversion": Inelastic scattering of ^{30}Ne and ^{36}Mg at intermediate energies

P. Doornenbal,[1,*] H. Scheit,[1,2,†] S. Takeuchi (武内聡),[1,‡] N. Aoi (青井考),[1,§] K. Li (李闊昂),[1,2] M. Matsushita (松下昌史),[1,3,∥] D. Steppenbeck,[1] H. Wang (王赫),[1,2] H. Baba (馬場秀忠),[1] E. Ideguchi (井手口栄治),[4,§] N. Kobayashi (小林信之),[5,**] Y. Kondo (近藤洋介),[5] J. Lee (李曉菁),[1,††] S. Michimasa (道正新一郎),[4] T. Motobayashi (本林透),[1] A. Poves,[6] H. Sakurai (櫻井博儀),[1] M. Takechi (武智麻耶),[1,‡‡] Y. Togano (栂野泰宏),[1,‡] and K. Yoneda (米田健一郎)[1]

[1]*RIKEN Nishina Center, Wako, Saitama 351-0198, Japan*
[2]*Peking University, Beijing 100871, People's Republic of China*
[3]*Department of Physics, Rikkyo University, Toshima, Tokyo 172-8501, Japan*
[4]*Center for Nuclear Study, University of Tokyo, RIKEN Campus, Wako, Saitama 351-0198, Japan*
[5]*Department of Physics, Tokyo Institute of Technology, Meguro, Tokyo 152-8551, Japan*
[6]*Departamento de Física Teorica and IFT-UAM/CSIC, Universidad Autónoma de Madrid, 28049 Madrid, Spain*

(Received 4 January 2016; published 11 April 2016)

The transition strengths of the first-excited 2^+ states and deformation lengths of the nuclei ^{30}Ne and ^{36}Mg were determined via Coulomb- and nuclear-force-dominated inelastic scattering at intermediate energies. Beams of these exotic nuclei were produced at the RIKEN Radioactive Isotope Beam Factory and were incident on lead and carbon targets at energies above 200 MeV/u. Absolute excitation cross sections on the lead target yielded reduced transition probabilities of 0.0277(79) and 0.0528(121) e^2 b^2, while the measurements with the carbon target revealed nuclear deformation lengths of $\delta_N = 1.98(11)$ and 1.93(11) fm for ^{30}Ne and ^{36}Mg, respectively. Corresponding quadrupole deformation parameters of $\beta_2 \sim 0.5$ from the two probes were found comparable in magnitude, showing no indication for a reduction in deformation along isotopic and isotonic chains from ^{32}Mg towards the neutron drip-line. Comparisons to shell-model calculations illustrate the importance of neutron excitations across the $N = 20$ shell for ^{30}Ne and suggest that shallow maximums of collectivity may occur around $N = 22$ and 24 along the neon and magnesium isotopic chains, respectively.

DOI: 10.1103/PhysRevC.93.044306

I. INTRODUCTION

The propagation of single-particle level energies from stable to exotic nuclei as function of the proton or neutron number is presently under investigation in many regions of the Segré chart. These studies have revealed that far away from the line of β stability traditional closed-shell numbers may vanish, while others can emerge [1]. For example, neutron shell quenching occurs around $N = 20$ [2–5] and $N = 28$ [6,7], while neutron numbers $N = 16$ and $N = 32$ and 34 have been found to feature doubly closed-shell signatures for ^{24}O and ^{52,54}Ca [8–11]. It has been shown that the creation and disappearance of magic numbers are mutually connected [12], raising the question of their respective region of validity. The $N = 20$ shell quenching was initially revealed by mass measurements yielding unusually high binding energies for the neutron-rich $Z = 11$ sodium isotopes ^{31,32}Na [2]. This mass anomaly led to the identification of an area of nuclei with $10 \leqslant Z \leqslant 12$ and $20 \leqslant N \leqslant 22$ for which $\nu(sd)^{-2}(fp)^2(2\hbar\omega)$ intruder configurations were anticipated to dominate the ground state of these systems [13]. Even though almost 40 years have passed since its discovery, the exact boundaries of this region, termed the "island of inversion" [14], as well as its propagation of collectivity remain unknown.

Experimentally, a large drop in excitation energy for the first-excited 2^+ state, $E(2_1^+)$, compared to neighboring, less neutron-rich nuclei nuclei was observed for ^{32}Mg [4] ($Z = 12, N = 20$) alongside an increased $E2$ excitation strength $B(E2)\uparrow$ [5]. Further investigations revealed also a large $B(E2)\uparrow$ for ^{34}Mg [15,16], while two-proton knockout reactions showed a low $E(2_1^+)$ for ^{36}Mg and that its ground state is dominated by $2\hbar\omega$ configurations [17]. Recently, the knowledge of the $E(2_1^+)$ and $E(4_1^+)$ values in the magnesium isotopes was extended up to $N = 26$, featuring a remarkable stability in the level energies [18]. These findings were interpreted as a merged $N = 20$ and $N = 28$ shell quenching, in agreement with shell-model calculations [19,20]. Accordingly, the neutron $0d_{3/2}, 0f_{7/2}$, and $1p_{3/2}$ orbits form a new (sub-)shell in the neutron-rich magnesium isotopes, resulting in the prediction of an inverted parabola $B(E2)\uparrow$ value pattern for mass $A = 30$–42 that peaks at ^{36}Mg [19,20].

In the chain of neon ($Z = 10$) isotopes, low $E(2_1^+)$ have been established for $N = 20$ and 22 [21–23]. They feature a gradual drop in $E(2_1^+)$ from $N = 16$ to $N = 20$ and suggest

*pieter@ribf.riken.jp
†Present address: Institut für Kernphysik, Technische Universität Darmstadt, Darmstadt, Germany.
‡Present address: Department of Physics, Tokyo Institute of Technology, Tokyo, Japan.
§Present address: Research Center for Nuclear Physics, Osaka University, Osaka, Japan.
∥Present address: Center for Nuclear Study, University of Tokyo, Tokyo, Japan.
**Present address: National Superconducting Cyclotron Laboratory, Michigan State University, East Lansing, MI, USA.
††Present address: Department of Physics, The University of Hong Kong, Hong Kong.
‡‡Present address: Graduate School of Science and Technology, Niigata University, Niigata, Japan.

 ©2016 American Physical Society

that ^{30,32}Ne belong to the island of inversion. However, the $E2$ excitation strengths for these two isotopes remain unknown. The most neutron-rich neon isotope with a measured $B(E2)\uparrow$ value is ^{28}Ne [24,25]; the more recent measurement [25] indicates no sign of enhanced collectivity despite an incipient drop of the $E(2_1^+)$. Theoretically, a $B(E2)\uparrow$ increase is expected when $N = 20$ is approached, and shell-model calculations [19,20,26–28] require inclusion of higher-lying orbits to reproduce the $E(2_1^+)$ value of ^{30}Ne. A first experimental hint in this direction was given by the increased nuclear deformation lengths (δ_N) observed in Refs. [21,29], suggesting large quadrupole deformation parameters (β_2, in the following abbreviated as β and distinguished as β_N and β_C for nuclear and electromagnetic parameters). The present work reports on Coulomb- and nuclear-force-dominated inelastic scattering measurements of ^{30}Ne and ^{36}Mg in order to further elucidate the $B(E2)\uparrow$ and deformation pattern in both isotopic chains at and beyond $N = 20$.

II. EXPERIMENTAL SETUP

The experiment was carried out at the Radioactive Isotope Beam Factory, operated by the RIKEN Nishina Center and the Center for Nuclear Study of the University of Tokyo. A ^{48}Ca primary beam was accelerated by the Superconducting Ring Cyclotron to an energy of 345 MeV/u and incident on a 15-mm beryllium target at the entrance of the BigRIPS fragment separator [30]. The average beam intensity at the production target was ~70 particle nA. Secondary ^{30}Ne and ^{36}Mg beams were produced by a filter combination of magnetic rigidity ($B\rho$) selection, energy loss by inserting a wedge-shaped aluminum degrader, and a second $B\rho$ selection in the first stage of BigRIPS. Two separate settings were necessary for the two secondary beams due to their different location in the Segré chart and restrictions on the maximum permissible particle rate in the present experiment. BigRIPS was set to its full momentum acceptance of ±3%.

The second stage of BigRIPS was used for event-by-event particle identification of the secondary beams by means of the $B\rho$-ΔE-TOF method: Two plastic scintillators were used to determine the time-of-flight (TOF), while the position and angle at the entrance of the second stage and the dispersive focus were measured with a set of parallel-plate avalanche counters (PPAC) [31] to determine $B\rho$. An energy loss measurement, ΔE, was conducted at the final focus of BigRIPS with an ionization chamber to determine the atomic number Z of the particles. For further separation, a second degrader was inserted at the second stage of BigRIPS. The beam intensities were 370 particles per second (pps) for ^{30}Ne and 95 pps for ^{36}Mg, and the corresponding beam cocktail purities were ~66% and 16%, respectively.

The secondary beams were incident on 3.37 g/cm^2 lead and 2.54 g/cm^2 carbon reaction targets to induce inelastic scattering dominated by Coulomb and nuclear excitation, respectively. At the center of the lead target, the average beam energies were 232 MeV/u for ^{30}Ne and 223 MeV/u for ^{36}Mg. For the carbon target, the respective energies were 228 and 218 MeV/u. Two PPACs were placed 1440 and 940 mm upstream and one PPAC was placed 875 mm downstream of the reaction target. The position resolution in X and Y of the PPACs was ~1 mm (σ), allowing us to determine the scattering angle with an accuracy of 5–6 mrad (σ). The secondary beams and reaction products were transported through the ZeroDegree spectrometer [30] to determine their atomic number Z and their mass-to-charge ratio A/Q using the same $B\rho$-ΔE-TOF method described above. Exemplary particle identification plots of BigRIPS and ZeroDegree for the ^{36}Mg beam impinging on the carbon target are shown in Fig. 1, demonstrating unambiguous separation for all beam constituents.

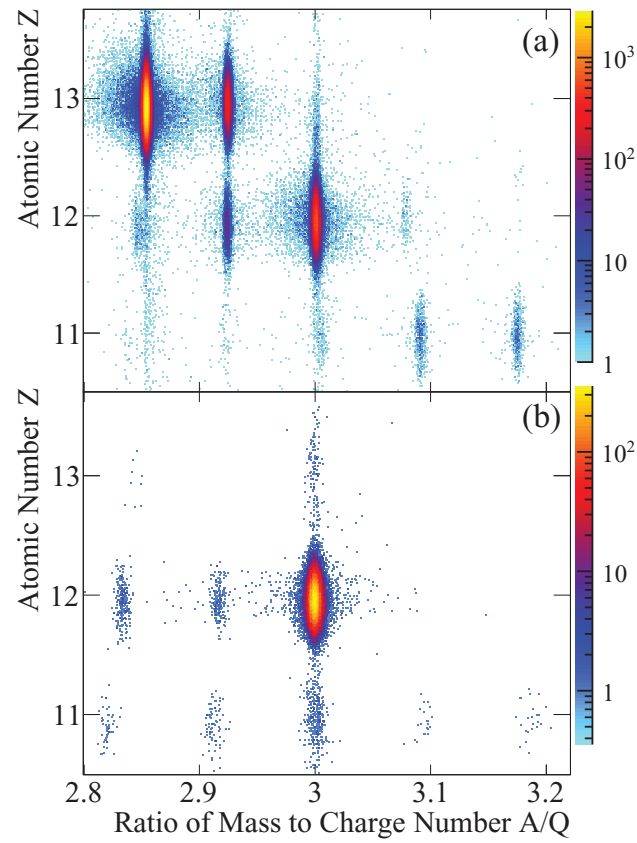

FIG. 1. Particle identification plot with the BigRIPS (a) and ZeroDegree (b) beam line detectors for the ^{36}Mg secondary beam setting impinging on the carbon reaction target. For panel (b), ^{36}Mg isotopes passing through BigRIPS were selected with a software cut.

The reaction target was surrounded by the DALI2 array [32] to detect deexcitation γ rays. It consisted of 186 large-volume NaI(Tl) detectors, covering inclination angles from 18° to 146° (center of crystals). Stationary ^{60}Co, ^{88}Y, and ^{137}Cs sources were used to deduce the full energy peak efficiency of DALI2. Measured efficiencies were in agreement ($\leqslant$6% error) with GEANT4 [33] simulations at the different γ-ray energies and determined to 16(1)% for events detected in single crystals at 1.33 MeV. The energy resolution after correcting for the Doppler shift was 10% for 1-MeV γ rays emitted at $\beta = 0.6$. Add-back was not applied. To reduce the contribution from the atomic background, the beam pipe was surrounded by a 1-mm-thick lead shield. Two triggers were employed to start the data taking: One trigger for coincidences between DALI2 and

particles passing through ZeroDegree and one scaled-down trigger (factor 1/20) for particles passing through BigRIPS to enable the normalization on the number of particles for cross-section determinations.

III. RESULTS

Doppler corrected γ-ray spectra measured in coincidence ($\pm$15 ns) with ^{30}Ne and ^{36}Mg identified in BigRIPS and ZeroDegree are displayed in Fig. 2 for both the Pb and C targets. For the lead target, the atomic background originated predominantly from secondary bremsstrahlung, which was emitted isotropically in the laboratory system up to energies of around 500 keV. Due to the atomic background, not all γ-ray emission angles were suitable to observe the $2_1^+ \rightarrow 0_{gs}^+$ transitions. Angular software cuts relative to the beam axis of $\vartheta \leqslant 82^\circ$ for ^{30}Ne and to $\vartheta \leqslant 65^\circ$ for ^{36}Mg were applied. With these angular cuts applied, the simulated efficiencies for 1-MeV γ rays emitted at $\beta = 0.6$ were 15% and 12%, respectively. The $2_1^+ \rightarrow 0_{gs}^+$ transition energies were determined to be 799(5) [801(6)] keV for ^{30}Ne and 666(5) [665(5)] keV for ^{36}Mg with the carbon (lead) targets, in agreement with the literature values [17,18,21,23]. Detector response curves were simulated with GEANT4 and took into account the intrinsic resolution of DALI2, the energy loss inside the target, and the γ-ray prolate (oblate) angular distributions for Coulomb (nuclear) excitation [34]. Also the γ-ray absorption by the reaction target was taken into account by the simulation, but was negligible due to the long lifetimes of the 2_1^+ states of interest and the software cuts of only forward angles for DALI2. Experimental data were then fitted with the intensity of the simulated response curves on top of two exponentials for the background, as shown in Fig. 2. Fit errors for the amplitude of the simulated response curves were around 5%. It is noted that cuts on different γ-ray emission angles within the ranges specified above for ^{30}Ne and ^{36}Mg yielded the same cross sections, implying that the simulated γ-ray angular distribution corresponded to the measured one. Conversely, the assumption of an isotropic γ-ray emission in the center-of-mass system would lead to about 10% higher cross sections.

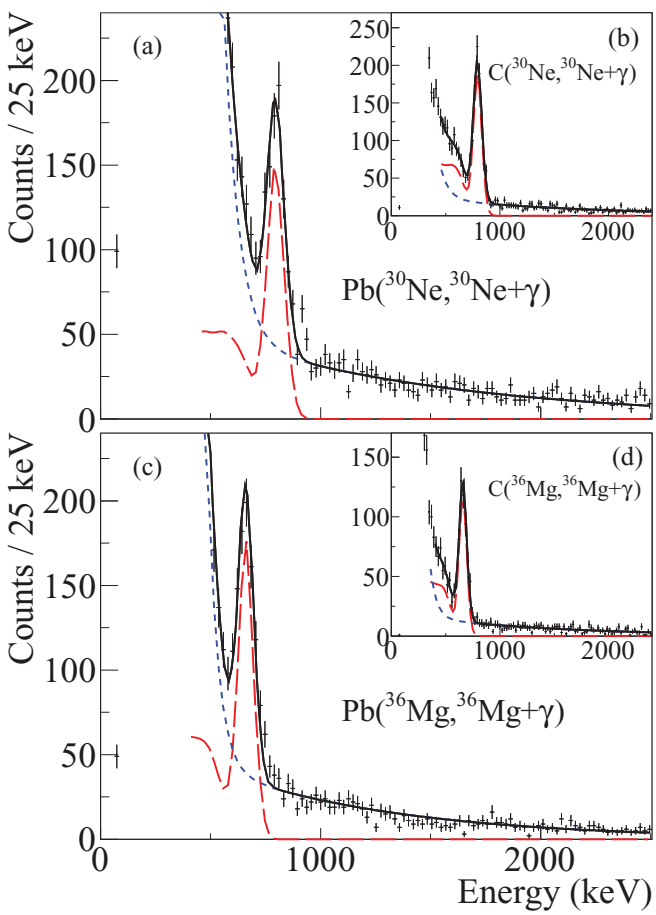

FIG. 2. Doppler-corrected γ-ray spectra for ^{30}Ne (a) and ^{36}Mg (c) from inelastic scattering on the lead target. Insets (b) and (d) show the respective measurements on the carbon target. Intensities were obtained by fitting the observed spectra with simulated line shapes (long dashed line) on top of two exponentials (short dashed line) for the background. The resulting fit curves are shown by the solid lines.

Cross sections of the 2_1^+ state on the carbon (lead) target were measured to be 15(1) [59(5)] mb for ^{30}Ne and 16(1) [77(6)] mbarn for ^{36}Mg. Quoted errors include the fit errors and the error for the absolute efficiency of DALI2, added in quadrature. For the observed cross sections, feeding from higher-lying 2^+ and 3^- states should be considered, even though no indication for such transitions was found in the Doppler-corrected spectra up to a limit of about 3% relative to the $2_1^+ \rightarrow 0_{gs}^+$ intensity. An analysis of the feeding from levels between 2 and 5 MeV for the well-known nucleus ^{32}Mg yielded 14(3)% at similar beam energies [35]. In the present case, the proximity of the neutron drip-line and the low neutron separation energies of 3430(300) and 3330(490) keV for ^{30}Ne and ^{36}Mg [36] should reduce this contribution by more than 50%. Due to the many ambiguities, a feeding of 6(6)% was assumed for all settings and subtracted from the observed cross sections.

To determine the deformation lengths and $B(E2)\uparrow$ values, the procedure outlined in Ref. [35] at similar beam energies was followed. Measured cross sections were compared to the calculations with the code ECIS97 [37] using the rotational model. The measured angular acceptance curve of ZeroDegree, the scattering angle resolution, and the angular straggling [38] were folded into the calculations. Due to the lack of experimental data in the region at the employed energies, only theoretically derived potentials were suitable. In the calculations, optical potentials derived from Ref. [39] were employed, which were demonstrated to lead to a good agreement with the known $B(E2)\uparrow$ value for ^{32}Mg in Ref. [35]. For inelastic scattering on the carbon target, respective nuclear deformation lengths of $\delta_N = 1.98(11)$ and 1.93(11) fm were determined for ^{30}Ne and ^{36}Mg, corresponding to nuclear deformation parameters of $\beta_N = 0.53(2)$ and 0.49(2), assuming the radius $R = 1.2A^{1/3}$ fm.

For the Pb target, agreement between calculated and measured cross sections was obtained for deformation lengths δ_C of 1.87(25) and 2.03(22) fm for ^{30}Ne and ^{36}Mg, resulting in $B(E2)\uparrow$ values of 0.0277(79) and 0.0528(121) e^2 b^2, when

TABLE I. Summary of observed $E(2_1^+)$ (in keV), feeding corrected cross sections $\sigma(2_1^+)$ (in mb), and deformation lengths δ (in fm) for ^{30}Ne and ^{36}Mg. The deformation lengths are presented by δ_N for the carbon and δ_C for the lead target, respectively. The corresponding deformation parameters β are calculated with $\beta = \delta/R$, using $R = 1.2A^{1/3}$ fm.

Projectile	Target	$E(2_1^+)$	$\sigma(2_1^+)$	δ	β
^{30}Ne	C	799(5)	14.4(14)	1.98(11)	0.53(3)
	Pb	801(6)	56(6)	1.87(25)	0.50(7)
^{36}Mg	C	666(5)	15.1(16)	1.93(11)	0.49(3)
	Pb	665(5)	72(8)	2.03(22)	0.51(6)

the relation $B(E2)\uparrow = (3ZeR^2/4\pi)^2\beta_C^2$, with $\beta_C = \delta_C/R$ and $R = 1.2A^{1/3}$ fm, is applied. The nuclear deformations obtained from the carbon target were included in the calculations. Errors originating from the measurements and the calculations include the errors of the fits of the experimental spectra, the measured absolute efficiency of DALI2 (6%), the applied feeding corrections (6%), the choice of optical potentials, the ZeroDegree transmission (3%), and the nuclear contributions. The errors were added in quadrature. Changing the potential depths and the diffuseness values in the theoretically derived optical potentials by values of 20% resulted in cross-section differences of less than 5%. Due to this robustness, an error of 5% was adopted for the choice of optical potential, which is comparable to the systematic error employed in Ref. [29] for the inelastic scattering on the hydrogen target. The assumption that $\delta_C = \delta_N$ would result in an ~8% higher $B(E2)\uparrow$ value for ^{30}Ne and an ~4% lower $B(E2)\uparrow$ value for ^{36}Mg. It is noted that the deformation length from scattering on hydrogen obtained in Ref. [29] of $\delta = 1.90(22)$ fm for ^{36}Mg agrees well with the present findings. However, the result of $\delta = 1.59(11)$ fm obtained in the same work for ^{30}Ne is lower than the present findings for the carbon target. A summary of the results obtained in the present work is provided in Table I.

IV. DISCUSSION

Figure 3 demonstrates that the present $B(E2)\uparrow$ value for ^{30}Ne extends the rise in $E2$ excitation strength along the $N = 20$ isotones from typical closed-shell values for ^{40}Ca, ^{38}Ar, ^{36}S, and ^{34}Si to the open-shell value for ^{32}Mg [5,48]. A first qualitative interpretation of the present findings for ^{30}Ne can be obtained from the N_pN_n scheme [40]. Predictions for $B(E2)\uparrow$ values can be obtained from this scheme based on a global fit as a function of the number of proton and neutron particles (holes) to the next closed shell. These predictions are displayed in Fig. 3 assuming a closed $N = 20$ shell ($N_n = 0$) and allowing for neutron excitations to the $0f_{7/2}$ and $1p_{3/2}$ shells ($N_n = 12$). A division into two distinct parts becomes apparent: The isotones ^{30}Ne and ^{32}Mg are well described with an open $N = 20$ shell, while for heavier isotones the shell remains closed.

It is also very instructive to follow experimental signatures for shell structure along isotopic chains. Figure 4 displays the $E(2_1^+)$, $E(4_1^+)$, and $B(E2)\uparrow$ values for neon isotopes as a function of neutron number. When approaching $N = 20$,

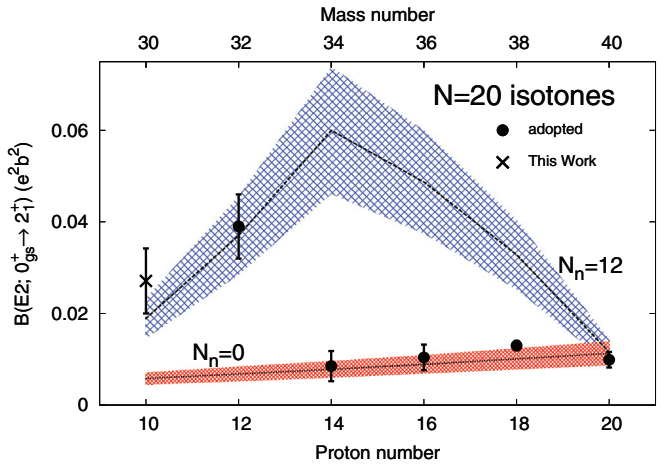

FIG. 3. $B(E2)\uparrow$ values along the $N = 20$ isotones in comparison to expectation values from the N_pN_n scheme [40] for $N_n = 0$ (dotted line) and $N_n = 12$ (dashed line). The hatched areas correspond to the scheme's fit errors. Adopted values are taken from Ref. [41].

a smooth, gradual drop in $E(2_1^+)$ is observed, in contrast to an increase expected for a good shell closure. While the $E2$ excitation strength trend is unclear from the measured data points for ^{26,28}Ne [24,25,47], the present value for ^{30}Ne establishes an enhanced collectivity. A similar experimental pattern is observed for the chain of magnesium isotopes, which is displayed in Fig. 5. Here, the decrease in $E(2_1^+)$ is more abrupt, as the energies for ^{28}Mg and ^{30}Mg are almost constant. Again the drop in $E(2_1^+)$ is correlated with an enhanced $B(E2)\uparrow$ value at $N = 20$. Beyond ^{32}Mg, the $E(2_1^+)$ and $E(4_1^+)$ values remain constant, while the maximum of the $E2$ excitation strength occurs at $N = 22$, which is in fact consistent with the value deduced in the present work at $N = 24$.

Theoretical works focusing on the *sd* shell and around the island of inversion are very abundant. When following the shell-model approach, notable progress includes the development of the SDPF-M [26] and SDPF-U-MIX [19,20] effective interactions, which, besides the *sd* shell for protons and neutrons, include the neutron $0f_{7/2}$ and $1p_{3/2}$ orbits for the former and the $1p_{1/2}$, $0f_{7/2}$, and $1p_{3/2}$ orbits for the latter in the model space to allow for neutron cross-shell excitations beyond $N = 20$. In contrast, the USD effective interaction and its more recent versions USDA/B [42,43] restrict the model space to the *sd* shell. A comparison of the $B(E2)\uparrow$ value for ^{30}Ne with these interactions reveals the importance of neutron excitations across $N = 20$.

Figures 4 and 5 include the theoretically predicted $E(2_1^+)$, $E(4_1^+)$, and $B(E2)\uparrow$ values from SDPF-M, SDPF-U-MIX, and USDA Hamiltonians. Different effective charges of $e_p = 1.3$ and $e_n = 0.5$ for SDPF-M, $e_p = 1.35$ and $e_n = 0.35$ for SDPF-U-MIX, and $e_p = 1.36$ and $e_n = 0.45$ for USDA were employed, as motivated by Refs. [19,20,26,50]. For the neon isotopes, good agreement with the experimental data is achieved for SDPF-M and SDPF-U-MIX for $E(2_1^+)$ and $E(4_1^+)$ values, while in the case of USDA, the $E(2_1^+)$ is predicted at almost 2 MeV. The pattern becomes more ambiguous for

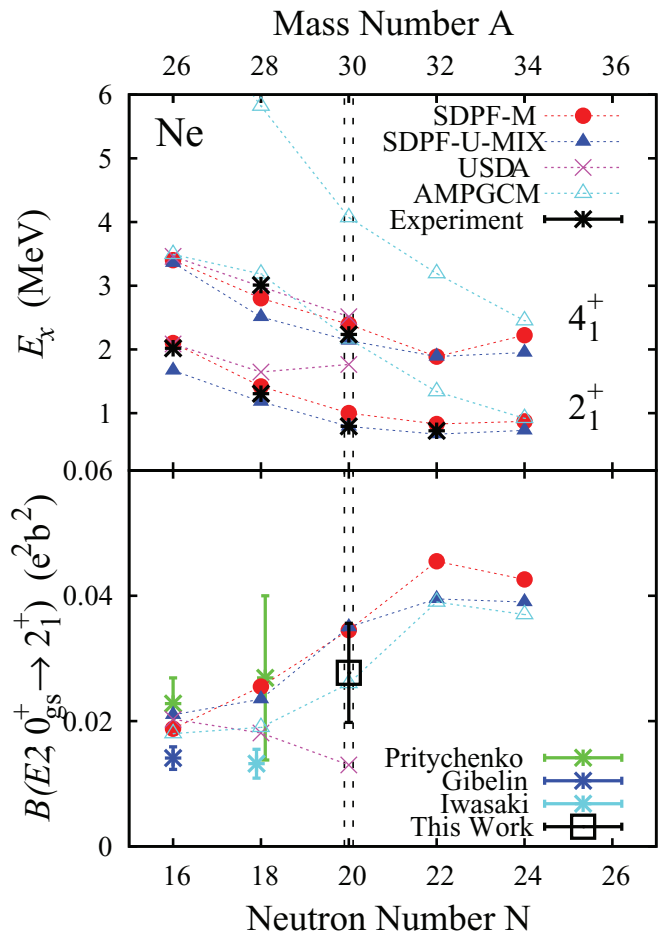

FIG. 4. Experimental $E(2_1^+)$ and $E(4_1^+)$ (top panel) and $B(E2)\uparrow$ (bottom panel) systematics for the neon isotopes. Shell-model predictions using the SDPF-M (red circles) [26], the SDPF-U-MIX (solid blue triangles) [19,20], and the USDA (purple crosses) [42,43] interactions as well as the mean-field-based approach AMPGCM (turquoise open triangles) [44–46] are compared to these data. Data points are taken from Refs. [21–25,41,47,48]. Lines are drawn to guide the eye.

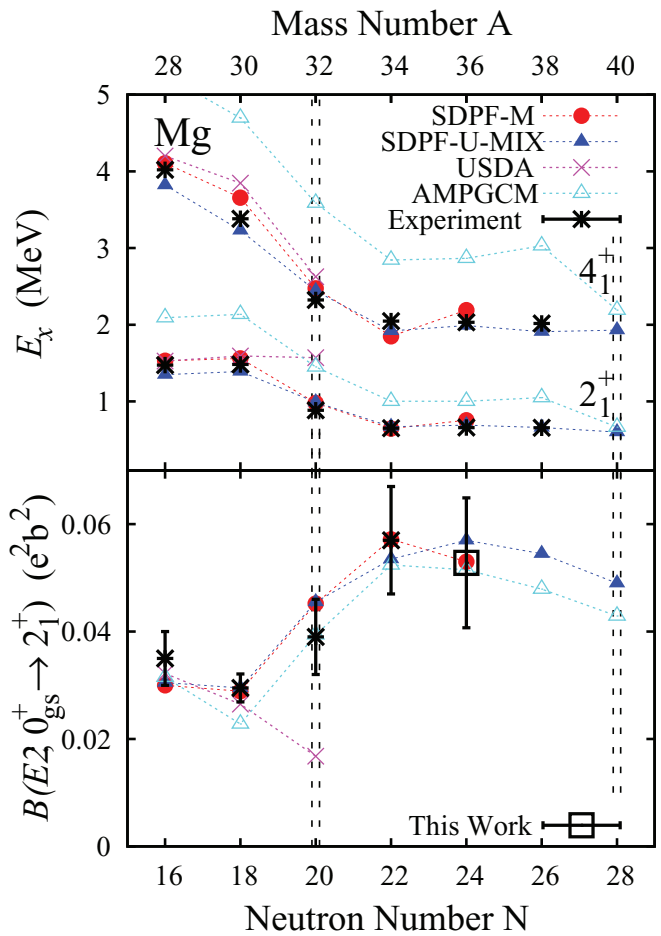

FIG. 5. Same as Fig. 4, but for magnesium isotopes. Data points are taken from Refs. [4,5,17,18,41,48,49].

the $B(E2)\uparrow$ values: Inconsistent experimental results were obtained for ^{26}Ne by Pritychenko *et al.* [24] and Gibelin *et al.* [47], while for ^{28}Ne the work by Iwasaki *et al.* [25], which agrees with the USDA calculation, supports a persistent $N = 20$ closed shell. This trend is broken by the present result for ^{30}Ne, though the predicted $B(E2)\uparrow$ values for SDPF-M and SDPF-U-MIX are somewhat larger but within the error bars. For ^{32}Ne, these calculations feature an increasing deformation parameter up to $\beta \sim 0.6$ for SDPF-M and up to $\beta \sim 0.57$ for SDPF-U-MIX, which may be larger than the experimental value. An evaluation of the cross section measured for this isotope on carbon in an earlier experiment [22] yields $\beta_N = 0.49(6)$, close to the present work for ^{30}Ne but less than the shell-model predictions.

A larger experimental data set is available for the chain of Mg isotopes, as all $E(2_1^+)$ and $E(4_1^+)$ values are known up to $N = 26$ and the present work extends the $B(E2)\uparrow$ values up to $N = 24$. A similar picture as for the neon isotopes arises for the trend of experimental values. Again, shell-model calculations using the SDPF-M and SDPF-U-MIX interactions are in in excellent agreement for the $E(2_1^+)$ and $E(4_1^+)$ values, whereas the $E(2_1^+)$ value at $N = 20$ cannot be reproduced with USDA. Good agreement between experiment and the SDPF-M and SDPF-U-MIX interactions is also obtained for the $B(E2)\uparrow$ values along the entire isotopic chain, in contrast to the neon isotopes. Maximum deformation is expected at around $^{34-36}$Mg with $\beta \sim 0.51$–0.55, thus lower than for the neon isotopes and within experimental reach. However, given the uncertainties of the present and the earlier work [15,16] as well as the anticipated shallow $B(E2)\uparrow$ maximum, the nucleus with maximum collectivity and/or deformation parameter remains unknown.

Conducted theoretical island of inversion studies based on the mean-field include the angular-momentum-projected generator coordinate method (AMPGCM) [44–46] using the Gogny interaction [51] with the parametrization D1S [52]. This approach implements configuration mixing at $N = 20$ and features prolate-deformed neutron-rich magnesium and neon isotopes. Calculation results are included in Figs. 4 and 5. For the magnesium isotopes, the general $E(2_1^+)$ and $E(4_1^+)$ trends are described well, though a factor of ~1.5 higher in excitation energy. The origin of a quenching factor of ~0.7

for the excitation energies has been discussed in Ref. [53] and attributed to the applied procedure. More importantly, calculated $B(E2)\uparrow$ provide an accurate description of the experimental values and their increase from $N = 20$. Similarly, the AMPGCM reproduces the observed $B(E2)\uparrow$ pattern in the neon isotopes better than the shell-model approach. However, calculated $E(2_1^+)$ and $E(4_1^+)$ values drop gradually from $N = 16$ to $N = 26$, while experiment indicates only little variance for the excitation energies for $N \geqslant 20$ [21–23].

V. SUMMARY

The $B(E2)\uparrow$ values and deformation lengths of ^{30}Ne and ^{36}Mg were determined via intermediate-energy inelastic scattering on lead and carbon targets at $\sim$230 MeV/u. Comparisons to state-of-the-art shell-model calculations showed that neutron excitations across the quenched $N = 20$ shell are necessary to reproduce the large excitation strength for ^{30}Ne. For ^{36}Mg, a similar $B(E2)\uparrow$ value to the $N = 22$ isotope ^{34}Mg was found, substantiating that large deformations of $\beta \sim 0.5$ are persistent beyond the originally proposed boundaries of the island of inversion. Furthermore, ^{30}Ne and ^{36}Mg yield the same deformation when studied by the two different probes, indicating that within the error bars $\delta_C = \delta_N$ for ^{30}Ne and for ^{36}Mg, respectively.

Overall, good agreement between theory and experiment is found for the magnesium isotopes. For the neon isotopes, perhaps due to scarce available data, the agreement is satisfactory but less pronounced. Here, the $B(E2)\uparrow$ trend from ^{26}Ne to ^{28}Ne could emerge as decisive for a detailed study of enhanced collectivity. More exotic neon and magnesium isotopes remain an interesting challenge, as the proximity of the neutron drip-line in these nuclei, not accounted for in Ref. [20], may influence their excitation energies and strengths. It has been found recently that the $N = 32$ subshell closure remains intact below the Ca isotopes [54,55] and theory prognoses a steep increase of 2_1^+ energies in Ne and Mg from $N = 28$ to $N = 32$ [20]. Owing to the developments in radioactive isotope beam science, measuring the onset of the expected drop in excitation strength may soon become feasible for magnesium isotopes.

ACKNOWLEDGMENTS

We thank the RIKEN Nishina Center accelerator department for providing a high intensity ^{48}Ca primary beam and the BigRIPS team for their efforts in preparing the secondary beams. A.P. is partly supported by MINECO (Spain) Grant No. FPA2014-57196 and Programme "Centros de Excelencia Severo Ochoa" SEV-2012-0249.

[1] O. Sorlin and M.-G. Porquet, Prog. Part. Nucl. Phys. **61**, 602 (2008).
[2] C. Thibault *et al.*, Phys. Rev. C **12**, 644 (1975).
[3] X. Campi, H. Flocard, A. Kerman, and S. Koonin, Nucl. Phys. A **251**, 193 (1975).
[4] C. Détraz, D. Guillemaud, G. Huber, R. Klapisch, M. Langevin, F. Naulin, C. Thibault, L. C. Carraz, and F. Touchard, Phys. Rev. C **19**, 164 (1979).
[5] T. Motobayashi *et al.*, Phys. Lett. B **346**, 9 (1995).
[6] B. Bastin *et al.*, Phys. Rev. Lett. **99**, 022503 (2007).
[7] S. Takeuchi *et al.*, Phys. Rev. Lett. **109**, 182501 (2012).
[8] C. Hoffman *et al.*, Phys. Lett. B **672**, 17 (2009).
[9] K. Tshoo *et al.*, Phys. Rev. Lett. **109**, 022501 (2012).
[10] F. Wienholtz *et al.*, Nature (London) **498**, 346 (2013).
[11] D. Steppenbeck *et al.*, Nature (London) **502**, 207 (2013).
[12] T. Otsuka, R. Fujimoto, Y. Utsuno, B. A. Brown, M. Honma, and T. Mizusaki, Phys. Rev. Lett. **87**, 082502 (2001).
[13] A. Poves and J. Retamosa, Phys. Lett. B **184**, 311 (1987).
[14] E. K. Warburton, J. A. Becker, and B. A. Brown, Phys. Rev. C **41**, 1147 (1990).
[15] H. Iwasaki *et al.*, Phys. Lett. B **522**, 227 (2001).
[16] J. A. Church *et al.*, Phys. Rev. C **72**, 054320 (2005).
[17] A. Gade *et al.*, Phys. Rev. Lett. **99**, 072502 (2007).
[18] P. Doornenbal *et al.*, Phys. Rev. Lett. **111**, 212502 (2013).
[19] A. Poves *et al.*, Phys. Scr. T **150**, 014030 (2012).
[20] E. Caurier, F. Nowacki, and A. Poves, Phys. Rev. C **90**, 014302 (2014).
[21] Y. Yanagisawa *et al.*, Phys. Lett. B **566**, 84 (2003).
[22] P. Doornenbal *et al.*, Phys. Rev. Lett. **103**, 032501 (2009).
[23] P. Fallon *et al.*, Phys. Rev. C **81**, 041302 (2010).
[24] B. Pritychenko *et al.*, Phys. Lett. B **461**, 322 (1999).
[25] H. Iwasaki *et al.*, Phys. Lett. B **620**, 118 (2005).
[26] Y. Utsuno, T. Otsuka, T. Mizusaki, and M. Honma, Phys. Rev. C **60**, 054315 (1999).
[27] T. Siiskonen, P. O. Lipas, and J. Rikovska, Phys. Rev. C **60**, 034312 (1999).
[28] E. Caurier, F. Nowacki, and A. Poves, Nucl. Phys. A **693**, 374 (2001).
[29] S. Michimasa *et al.*, Phys. Rev. C **89**, 054307 (2014).
[30] T. Kubo *et al.*, Prog. Theor. Exp. Phys. **2012**, 03C003 (2012).
[31] H. Kumagai *et al.*, Nucl. Instrum. Methods Phys. Res., Sect. A **470**, 562 (2001).
[32] S. Takeuchi *et al.*, Nucl. Instrum. Methods Phys. Res., Sect. A **763**, 596 (2014).
[33] S. Agostinelli *et al.*, Nucl. Instrum. Methods Phys. Res., Sect. A **506**, 250 (2003).
[34] H. Olliver, T. Glasmacher, and A. E. Stuchbery, Phys. Rev. C **68**, 044312 (2003).
[35] K. Li *et al.*, Phys. Rev. C **92**, 014608 (2015).
[36] G. Audi *et al.*, Chin. Phys. C **36**, 1287 (2012).
[37] J. Raynal, coupled-channel code ECIS97 (unpublished).
[38] ATIMA code, http://web-docs.gsi.de/~weick/atima/.
[39] T. Furumoto, W. Horiuchi, M. Takashina, Y. Yamamoto, and Y. Sakuragi, Phys. Rev. C **85**, 044607 (2012).
[40] R. F. Casten and N. V. Zamfir, Phys. Rev. Lett. **70**, 402 (1993).
[41] S. Raman, Jr., C. W. N., and P. Tikkanen, At. Data Nucl. Data Tables **78**, 1 (2001).
[42] B. A. Brown *et al.*, Ann. Phys. **182**, 191 (1988).
[43] B. A. Brown and W. A. Richter, Phys. Rev. C **74**, 034315 (2006).
[44] R. Rodríguez-Guzmán, J. Egido, and L. Robledo, Phys. Lett. B **474**, 15 (2000).
[45] R. Rodríguez-Guzmán, J. Egido, and L. Robledo, Nucl. Phys. A **709**, 201 (2002).

[46] R. Rodríguez-Guzmán, J. Egido, and L. Robledo, Eur. Phys. J. A **17**, 37 (2003).
[47] J. Gibelin *et al.*, Phys. Rev. C **75**, 057306 (2007).
[48] Ensdf Database, http://www.nndc.bnl.gov/ensdf/.
[49] K. Yoneda *et al.*, Phys. Lett. B **499**, 233 (2001).
[50] W. A. Richter, S. Mkhize, and B. A. Brown, Phys. Rev. C **78**, 064302 (2008).
[51] J. Dechargé and D. Gogny, Phys. Rev. C **21**, 1568 (1980).
[52] J. Berger, M. Girod, and D. Gogny, Nucl. Phys. A **428**, 23 (1984).
[53] R. R. Rodríguez-Guzmán, J. L. Egido, and L. M. Robledo, Phys. Rev. C **62**, 054319 (2000).
[54] M. Rosenbusch *et al.*, Phys. Rev. Lett. **114**, 202501 (2015).
[55] D. Steppenbeck *et al.*, Phys. Rev. Lett. **114**, 252501 (2015).